ROYAL SOCIETY
OF CHEMISTRY

PAPER

Check for updates

Electronic and defect properties of (CH₃NH₃)₂Pb(SCN)₂I₂ analogues for photovoltaic applications†

Alex M. Ganose,[ab] Christopher N. Savory[a] and David O. Scanlon [ID] *[ab]

In the past 5 years, hybrid halide perovskites have emerged as a class of highly efficient photovoltaic (PV) absorbers, with excellent electronic properties and low cost synthesis routes. Unfortunately, despite much research effort, their long-term stability is poor and presents a major obstacle toward commercialisation. The layered perovskite (CH₃NH₃)₂Pb(SCN)₂I₂ (MAPSI) has recently been identified as a promising PV candidate material due to its enhanced stability and favourable electronic properties. Here, we demonstrate, using relativistic hybrid density functional theory, that the MAPSI structural motif can be extended to include a range of other metals, halides and even pseudohalides. In this way, the electronic structure of MAPSI can be tuned without affecting its stability with respect towards decomposition. These results indicate the possibility of lead-free MAPSI analogues, with suitable properties for photovoltaic top cells in tandem devices.

1   Introduction

The emergence of CH₃NH₃PbI₃ (MAPI) in 2009 sparked an explosion of interest into lead–halide perovskites as efficient, cheap, and easy to manufacture solar absorbers.[1–3] The excitement surrounding the lead–halide perovskites stems from their rapid and seemingly inexorable rise in power conversion efficiencies (PCEs)—from 4% to 22% in just 6 years.[4] Indeed, MAPI can be viewed as an overnight success compared to other absorber technologies, which have required several decades' development to achieve comparable efficiencies. This intense progress has been enabled by an exceptional combination of electronic and photophysical properties, such as an ideal band gap of 1.55 eV,[5] strong optical absorption, small exciton binding energies,[6] ambipolar charge transport,[7–10] and high defect tolerance.[11] Furthermore, the ability of inexpensive solution-processing methods to produce high-quality thin films enables facile fabrication scale-up through roll-to-roll printing.[12–14]

Despite significant progress in optimising device architectures and deposition conditions, poor long-term stability remains a major roadblock in the commercialisation of lead–halide perovskites.[1,15] While device encapsulation should prevent decomposition by air and moisture, hybrid perovskites have been shown to degrade when exposed to moderate heat or even prolonged illumination.[16–18] Recently, several studies, both theoretical and experimental, have indicated that MAPI is intrinsically unstable with respect to phase separation into PbI₂ and CH₃NH₃I₃, due to its small formation energy.[19–22] Attempts to find novel compositions with enhanced stabilities have met with little success, in part due to the limited number of potential cations capable of replacing methylammonium (MA) in the perovskite structure.[23,24] A recently revised tolerance factor, taking into account the increased covalency seen in some metal–halide bonds, suggests that only a handful of hybrid perovskites remain to be discovered, with most expected to show unsuitable electronic properties for photovoltaic applications.[25] Such studies highlight the pressing need to move beyond the cubic perovskite motif if alternative schemes to improve stability are to be developed.[4,26]

Layered hybrid perovskites—which can be formed when the organic cation is too bulky to fit within the perovskite cage—have attracted attention due to their enhanced moisture stability.[4,27,28] Despite impressive advances in their efficiencies, with 15.3% reached in 2016,[29] layered perovskites typically possess relatively large band gaps in the range 2.6–2.9 eV and high exciton binding energies around 300 meV.[30,31] Recently, partial substitution of iodide with thiocyanate (SCN) to form (CH₃NH₃)₂Pb(SCN)₂I₂ (MAPSI) has been proposed as an alternative route to improved chemical stability,[22,32] with device efficiencies up to 8.3% reported for mixed MAPSI/MAPI cells.[32,33] MAPSI also crystallises in a two-dimensional (2D) layered structure, with Pb octahedrally coordinated to four equatorial I and two axial SCN, with the MA sandwiched between the layers (Fig. 1).[34]

[a]Department of Chemistry, University College London, 20 Gordon Street, London WC1H 0AJ, UK. E-mail: d.scanlon@ucl.ac.uk; Tel: +44(0) 1234 567 890

[b]Diamond Light Source Ltd., Diamond House, Harwell Science and Innovation Campus, Didcot, Oxfordshire OX11 0DE, UK

† Electronic supplementary information (ESI) available: Effect of spin–orbit coupling, band structures and transition level diagrams. See DOI: 10.1039/c7ta01688c
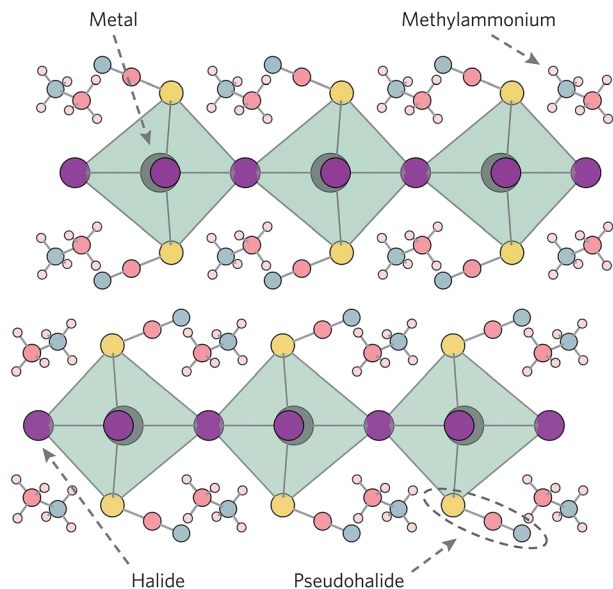
This journal is © The Royal Society of Chemistry 2017

J. Mater. Chem. A, 2017, 5, 7845–7853 | 7845

Fig. 1 Crystal structure of $(CH_3NH_3)_2Pb(SCN)_2I_2$ viewed along the [001] direction. Pb, I, S, C, N, and H atoms denoted by dark grey, purple, yellow, red, blue, and pink spheres, respectively. The octahedral nature of Pb is illustrated using green polyhedra.

There have been conflicting reports as to the magnitude of MAPSI's optical band gap: initial studies indicated a direct optical gap of 1.57 eV,[34,35] however, work by Xiao et al. showed thin films with indirect and direct optical band gaps of 2.04 eV and 2.11 eV, respectively.[36] A recent paper by Umeyama et al. further reported a larger band gap for MAPSI, finding a red-to-black piezochromic response upon compression (2.6 GPa).[37] While the exact nature of this disparity has yet to be resolved, it has been suggested that contamination of MAPSI thin films with small concentrations of MAPI may be a factor. Alternatively, Younts et al. have demonstrated highly efficient triplet state formation in MAPSI, with phosphorescence over 47 times more intense than band gap fluorescence.[38] This triplet peak occurs at 1.64 eV and helps to explain some of the previous photoluminescence results that have obfuscated band gap determination.[33] Regardless, a band gap of ~2.1 eV and exciton binding energies less than 200 meV (ref. 37) are unusual for 2D perovskites and make MAPSI a compound of interest for a top cell absorber in tandem devices, where perovskite/silicon cells have recently reached efficiencies of 23.6%.[39]

Recent theoretical research into the electronic structure of MAPSI has revealed many similarities to the electronic structure of MAPI.[22,36,40] MAPSI possesses small effective masses of both holes ($0.20m_0$) and electrons ($0.14m_0$) for directions parallel to the perovskite sheets, thereby promoting high carrier mobilities in these directions.[22] Furthermore, Rashba splitting in the lower conduction band, and to a lesser extent in the upper valence band, results in the formation of a spin-split indirect gap, which has recently been implicated in reducing radiative recombination by a factor of over 350 in MAPI.[41,42] Defect calculations have revealed that the Fermi level of MAPSI is highly tunable based on synthesis conditions, with a lead poor/iodine rich environment desirable to produce p-type samples dominated by shallow defects.[40]

The confirmation of MAPSI as a suitable absorber material for photovoltaic top cells opens up some fundamental questions. Similarly to the ABX_3 structured perovskites, which can be tuned on the A, B and X sites,[43] can MAPSI also function as a parent compound to a range of analogues possessing the same structural motif? Chemically, it should be viable to replace Pb with other 2+ cations such as Sn, I with Cl and Br, and SCN with other pseudohalides such as OCN and SeCN. Indeed, Sn^{2+} has recently been described as the "chameleon" of the p-block elements, based on its versatility in forming new structure types.[44] In this report we therefore look beyond MAPSI to consider a total of 17 analogue compounds, comprising all possible compositions of $(CH_3NH_3)_2MPs_2X_2$ (where M = Sn, Pb; Ps = OCN, SCN, SeCN; and X = Cl, Br, I). Relativistic hybrid density functional theory (DFT) is used to assess these analogues for their fundamental solar absorber properties, including band structures and effective masses. Band alignment calculations indicate that hole and electron contact materials commonly used in devices containing the cubic perovskites should still perform well, despite a decrease in ionisation potential and electron affinity. Lastly, defect calculations reveal that most intrinsic vacancy defects possess relatively shallow transition levels that should not participate in trap-assisted recombination.

2 Computational methodology

All calculations were carried out in the framework of density functional theory, using the Vienna Ab initio Simulation Package (VASP),[45–48] with the projector augmented-wave (PAW) method used to describe the interactions between core and valence electrons.[49] For the 50 atom unit cell of $(CH_3NH_3)_2M(Ps)_2X_2$, a k-point sampling of Γ-centred $1 \times 4 \times 4$ was necessary to achieve convergence to 1 meV per atom. The plane wave cut-off was converged to within 10 meV per atom, with a cut-off energy of 400 eV found to be sufficient. During geometry optimisation, the plane wave cut-off was raised to 520 eV to prevent basis set errors resulting in Pulay stress.[50] The structures were considered converged when all forces totalled less than 10 meV $Å^{-1}$. Geometry relaxations were performed using the PBEsol functional,[51] a version of the Perdew Burke and Ernzerhof (PBE) functional[52] revised for solids. PBEsol has been shown to accurately reproduce the structure parameters of many materials containing weak dispersive interactions (as present across the layers in MAPSI), without requiring an additional dispersion correction.[53,54]

Due to the propensity for functionals based on the generalised gradient approximation (GGA) to severely underestimate band gaps, the Heyd–Scuseria–Ernzerhof hybrid functional (HSE06) was employed.[55,56] Furthermore, explicit treatment of spin orbit coupling (SOC) effects is essential to account for the relativistic effects seen in the Sn, Pb, and I p orbitals.[57,58] This combination of HSE06 with SOC has been shown to provide an accurate description of the electronic structures for many bismuth and lead containing solar absorbers and was therefore

used during density of states and band structure calculations.[59–62] The Brillouin zone for the $Pnm2_1$ space group, illustrating the relevant high symmetry points, is provided in Fig. S1 of the ESI.† Dielectric constants were calculated using the PBEsol functional using density functional perturbation theory (DFPT),[63] with a denser k-point mesh of Γ-centred $3 \times 6 \times 6$ necessary to reach convergence.

In order to align the electronic eigenvalues to the vacuum level—and thus calculate ionisation potentials and electron affinities—a slab model was constructed containing 30 Å of vacuum and a 25 Å slab. The MacroDensity package was used to extract and plot the corresponding Hartree potential along the c-direction.[64–66] The reference for the vacuum level was taken as the energy of the potential at the plateau of the potential. Whilst HSE06 + SOC is known to provide accurate ionisation potentials for other lead and bismuth based absorbers, its use in this report was untenable due to the large size of the slab model employed.[67] Slab calculations were instead performed using the HSE06 functional with an explicit correction for the band gap and VBM energy taken from the bulk, calculated using HSE06 + SOC. The (100) surface was chosen as it resulted in a non-polar, low energy termination due to the absence of any dangling bonds.

Defects were calculated in a $1 \times 3 \times 3$ (450 atom) supercell using the PBEsol functional. Several corrections were applied, including a correction to account for potential alignment mismatch between the host and defective supercell.[68] The introduction of a defect in finite periodic repeating image causes an impurity–impurity interaction resulting in the formation of a defect band.[68,69] If this band hybridises with a conduction or valence band in the material, a band filling correction, E_{bf}, is necessary to resolve the effects of erroneous band dispersion and band filling on the total energy.[68] Furthermore, a correction for charged defects, E_{icc}, is required due to the slow decay of coulombic interactions with distance, causing spurious interactions between defect charge sites in neighbouring cells.[70] We have used the formalism developed by Murphy et al., which properly accounts for any anisotropy in the dielectric properties of the system.[71] The thermodynamic transition level, $\varepsilon(D, q/q')$—i.e. the energy at which the charge state of defect, D, spontaneously transforms from $q \leftrightarrow q'$ — was calculated according to:

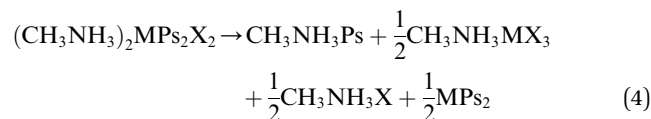$$\varepsilon\left(D, q/q'\right) = \frac{E^{D,q} - E^{D,q'}}{q' - q} \quad (1)$$

3 Results and discussion

The starting point for all geometry relaxations was the experimental structure of $(CH_3NH_3)_2Pb(SCN)_2I_2$ relaxed using PBEsol. For each composition of $(CH_3NH_3)_2MPs_2X_2$ (where M = Sn, Pb; Ps = OCN, SCN, SeCN; and X = Cl, Br, I) the appropriate elements were substituted into the structure, before a PBEsol geometry optimisation was performed. As all replacement elements are isoelectronic with their counterparts, the geometric structure was expected to remain relatively

unperturbed. Indeed, all compounds retained the orthorhombic $Pnm2_1$ space group of MAPSI,[34] with only subtle distortions of the local bonding observed (the relaxed structures for all analogues are provided in an online repository).[72]

3.1 Stabilities

To test the of stability of these materials, we have calculated the enthalpy of decomposition for several routes, analogous to those considered previously for MAPSI. For $(CH_3NH_3)_2MPs_2X_2$ (where M = Sn, Pb; Ps = OCN, SCN, SeCN; and X = Cl, Br, I) the decomposition routes considered were:

$$(CH_3NH_3)_2MPs_2X_2 \rightarrow 2CH_3NH_3X + MPs_2 \quad (2)$$

$$(CH_3NH_3)_2MPs_2X_2 \rightarrow 2CH_3NH_3Ps + MX_2 \quad (3)$$

$$(CH_3NH_3)_2MPs_2X_2 \rightarrow CH_3NH_3Ps + \frac{1}{2}CH_3NH_3MX_3 + \frac{1}{2}CH_3NH_3X + \frac{1}{2}MPs_2 \quad (4)$$

The enthalpies of decomposition, $\Delta_d H$, for all analogues and decomposition pathways are provided in Table 1. All compounds showed positive enthalpies of decomposition across all decomposition routes, indicating that they should be stable with respect to phase separation. This is in contrast to MAPI, for which theoretical and experimental results suggest spontaneous decomposition into CH_3NH_3I and PbI_2 is favourable.[20–22]

3.2 Electronic properties

The fundamental direct and indirect band gaps for all analogues, calculated using HSE06 + SOC, are provided in Table 2. We note that, based on previous theoretical investigations

Table 1 Enthalpy of decomposition, $\Delta_f H$, with respect to eqn (2)–(4), for $(CH_3NH_3)_2MPs_2X_2$, where M = Sn, Pb; Ps = OCN, SCN, SeCN; and X = Cl, Br, I, calculated using PBEsol

	Compound	$\Delta_d H$ (eV)		
		Eqn (2)	Eqn (3)	Eqn (4)
Pb	$MA_2Pb(OCN)_2Cl_2$	0.05	2.66	0.72
	$MA_2Pb(SCN)_2Cl_2$	0.08	2.99	0.90
	$MA_2Pb(SeCN)_2Cl_2$	0.11	3.23	1.03
	$MA_2Pb(OCN)_2Br_2$	0.10	0.63	0.85
	$MA_2Pb(SeCN)_2Br_2$	0.25	1.29	1.25
	$MA_2Pb(OCN)_2I_2$	0.13	1.41	0.79
	$MA_2Pb(SCN)_2I_2$	0.38	1.97	1.20
	$MA_2Pb(SeCN)_2I_2$	0.41	2.21	1.33
Sn	$MA_2Sn(OCN)_2Cl_2$	4.09	1.62	2.78
	$MA_2Sn(SCN)_2Cl_2$	0.16	2.09	1.04
	$MA_2Sn(SeCN)_2Cl_2$	0.11	2.31	1.13
	$MA_2Sn(OCN)_2Br_2$	4.19	1.66	2.87
	$MA_2Sn(SCN)_2Br_2$	0.22	2.09	1.10
	$MA_2Sn(SeCN)_2Br_2$	0.18	2.31	2.31
	$MA_2Sn(OCN)_2I_2$	4.19	1.46	2.85
	$MA_2Sn(SCN)_2I_2$	0.34	2.01	1.20
	$MA_2Sn(SeCN)_2I_2$	0.32	2.25	1.31

This journal is © The Royal Society of Chemistry 2017

J. Mater. Chem. A, 2017, **5**, 7845–7853 | **7847**

into MAPSI demonstrating that the HSE06 + SOC band gap is ~0.3 eV smaller than the reported optical gap, the calculated band gaps for all analogues are likely to be underestimated relative to the room temperature optical gaps.[22,36] Unlike in MAPSI, where the fundamental band gap is direct, most of the analogues possess slightly indirect gaps. However, the difference between direct and indirect transitions is small—between 10–40 meV—and should therefore have a limited effect on the strength of optical absorption.[4]

The magnitude of the band gaps appears to be controlled mainly by the X site anion: as the halide changes moving down group 17, the band gap narrows from ~3.0 eV (Cl) to ~2.4 eV (Br) and ~1.8 eV (I). In MAPSI, the valence band maximum (VBM) is composed almost entirely of halide p states with some pseudohalide contributions, whereas the conduction band is dominated by Pb p states.[22] As such, the valence band composition appears to control the band gap reduction down the series, in line with the binding energy of the halide p orbitals. The pseudohalide also has a small effect on the band gap, with the cyanate analogues in general showing larger band gaps than their thiocyanate and selenocyanate counterparts. Additionally, the tin analogues possess band gaps an average of 0.40 eV smaller than the corresponding lead compounds, reflecting the increase in binding energy of the lead 6s orbitals, which are stabilised due to relativistic contraction of the s shell, and act to lower the valence band maximum. However, the trends seen across both the pseudohalides and metals are not observed in the band gaps of the iodides, which show little correlation to composition. Of the complete set of analogues, the iodides all possess direct band gaps suitable for photovoltaic top cells (1.69–1.92 eV), when considering the likely underestimation of the HSE06 + SOC results.

The effect of spin–orbit coupling on the band structures was tested, with the full results provided in Table S1 of the ESI.† The relativistic renormalisation of the band gap was significantly larger in the lead (~0.6–0.9 eV) than the tin (~0.1–0.2 eV) analogues, as expected as SOC interactions scale approximately as Z^4. Regardless, our results indicate the importance of proper treatment of relativistic effects when modelling these systems.

To illustrate the effect of the halide on electronic properties, the band structures for a selection of the lead and tin cyanate analogues—namely $(CH_3NH_3)_2M(OCN)_2X_2$ where X = Cl and I, and M = Pb and Sn—are given in Fig. 2 (the full set of band structures for each composition can be found in Fig. S2 and S3 of the ESI†). The reduction in band gap going down group 17 can be seen clearly, with the width of the conduction and valence bands staying relatively constant across all compositions. The VBM in both the lead and tin chlorides is found at the R point $(\bar{0.5}, 0.5, 0.5)$. When moving to the bromides and iodides, the VBM is shifted slightly to the side of the R or U $\left(0, \frac{1}{2}, \frac{1}{2}\right)$ points due to increased Rashba splitting of the upper valence bands. Conversely, the position of the conduction band minimum (CBM) shows little correlation to the halide and is found near to either the R or U point depending on the anisotropy in Rashba splitting. The lowering of the band gap is accompanied by a reduction in the effective masses of both holes and electrons for the directions parallel to the 2D perovskite sheets ($m^{\parallel}$, in the [010] and [001] directions), with $m_h^{\parallel} = 0.59 m_0$, $0.34 m_0$, and $0.22 m_0$ and $m_e^{\parallel} = 0.42 m_0$, $0.28 m_0$, $0.18 m_0$ for Cl, Br, and I lead cyanates, respectively. The effective masses for the directions perpendicular to the perovskite sheets ([100]) are large (~$40 m_0$), reflecting the weak interactions spanning the 2D layers.

To demonstrate the role of the pseudohalide on electronic properties, the band structures for a selection of the tin bromide and iodide analogues—$(CH_3NH_3)_2Sn(Ps)_2X_2$ where Ps = OCN and SeCN, and X = Br and I—are given in Fig. 3. Moving down

Table 2 Electronic properties of $(CH_3NH_3)_2MPs_2X_2$, where M = Sn, Pb; Ps = OCN, SCN, SeCN; and X = Cl, Br, I, calculated using HSE06 + SOC. Indirect and direct band gaps denoted by E_g^{ind} and E_g^{dir}, respectively. Hole and electron effective masses are given by m_h and m_e, and the dielectric constant is indicated by ε_r. IP and EA stand for ionisation potential and electron affinity, respectively. ⊥ and ∥ indicate properties perpendicular and parallel to the 2D perovskite sheets, respectively

	Compound	E_g^{ind} (eV)	E_g^{dir} (eV)	$m_h^{\perp}$ (m_0)	$m_h^{\parallel}$ (m_0)	$m_e^{\parallel}$ (m_0)	$\varepsilon_r^{\perp}$	$\varepsilon_r^{\parallel}$	IP (eV)	EA (eV)
Pb	MA$_2$Pb(OCN)$_2$Cl$_2$	3.47	3.51	41.10	0.59	0.42	7.2	11.4	7.14	3.67
	MA$_2$Pb(SCN)$_2$Cl$_2$	3.03	3.05	40.00	3.07	0.50	6.6	19.5	6.50	3.94
	MA$_2$Pb(SeCN)$_2$Cl$_2$	3.04	3.05	38.89	14.09	0.59	6.4	19.0	5.68	3.93
	MA$_2$Pb(OCN)$_2$Br$_2$	2.56	2.58	—	0.34	0.28	8.4	9.1	6.38	3.34
	MA$_2$Pb(SCN)$_2$Br$_2$	2.30	2.32	36.17	0.44	0.25	8.3	19.6	6.03	3.73
	MA$_2$Pb(SeCN)$_2$Br$_2$	2.31	2.33	—	1.89	0.29	7.4	16.8	5.55	3.76
	MA$_2$Pb(OCN)$_2$I$_2$	1.75	1.76	—	0.22	0.18	9.3	8.5	6.27	3.23
	MA$_2$Pb(SCN)$_2$I$_2$	1.79	1.79	—	0.31	0.20	9.0	21.9	5.91	3.60
	MA$_2$Pb(SeCN)$_2$I$_2$	1.82	1.85	—	0.86	0.19	9.2	17.7	5.51	3.68
Sn	MA$_2$Sn(OCN)$_2$Cl$_2$	4.03	4.05	39.52	1.36	0.63	9.3	6.1	6.67	2.64
	MA$_2$Sn(SCN)$_2$Cl$_2$	3.74	3.74	38.74	20.42	0.96	6.9	7.0	5.94	2.88
	MA$_2$Sn(SeCN)$_2$Cl$_2$	3.56	3.57	37.59	38.66	0.86	7.0	11.7	5.13	3.22
	MA$_2$Sn(OCN)$_2$Br$_2$	3.06	3.08	—	0.36	0.43	12.5	7.2	6.06	2.32
	MA$_2$Sn(SCN)$_2$Br$_2$	2.98	2.98	—	2.15	0.63	8.3	8.4	5.67	2.69
	MA$_2$Sn(SeCN)$_2$Br$_2$	2.96	2.96	—	3.85	0.64	8.5	20.2	4.79	3.12
	MA$_2$Sn(OCN)$_2$I$_2$	1.90	1.92	—	0.19	0.32	9.3	6.9	5.90	2.33
	MA$_2$Sn(SCN)$_2$I$_2$	1.67	1.69	—	0.51	0.32	8.7	7.8	5.64	2.67
	MA$_2$Sn(SeCN)$_2$I$_2$	1.89	1.89	—	0.84	0.38	8.8	13.9	4.94	3.06

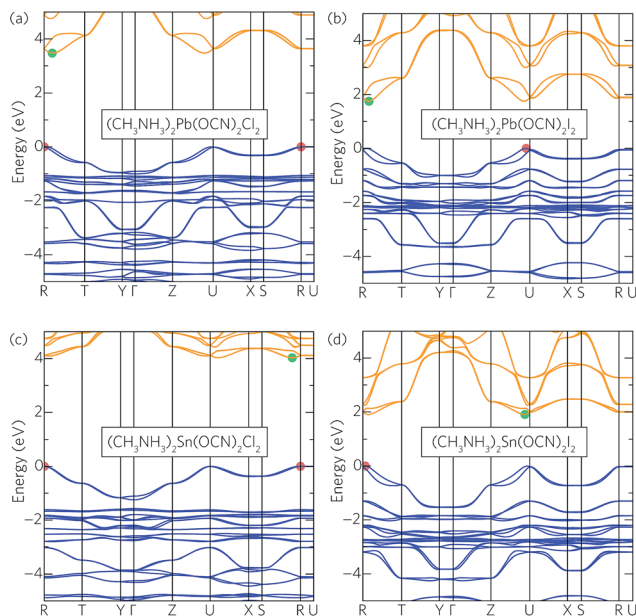**Fig. 2** Effect of halide on electronic structure. HSE06 + SOC calculated band structure of MAPSI-structured cyanate compounds: (a) $(CH_3NH_3)_2Pb(OCN)_2Cl_2$, (b) $(CH_3NH_3)_2Pb(OCN)_2I_2$, (c) $(CH_3NH_3)_2Sn(OCN)_2Cl_2$, and (d) $(CH_3NH_3)_2Sn(OCN)_2I_2$. The valence band maximum is set to 0 eV. Valence and conduction bands indicated by blue and orange lines, respectively. Green and red circles indicate the valence band maximum and conduction band minimum.
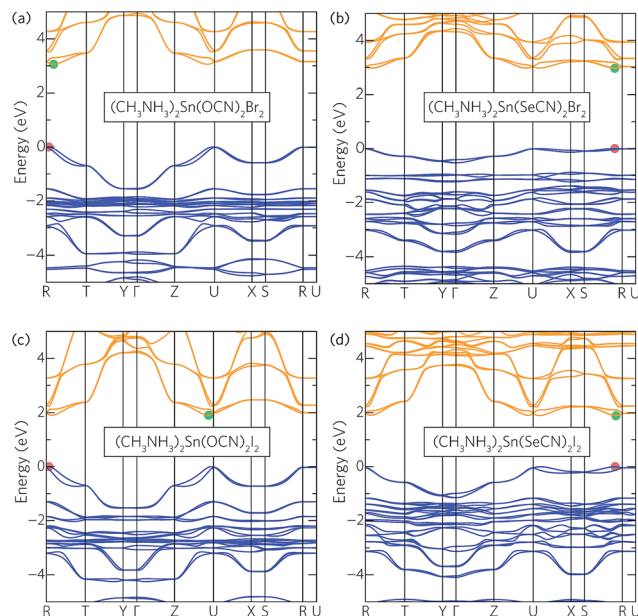
Fig. 3 Effect of pseudohalide on electronic structure. HSE06 + SOC calculated band structure of MAPSI-structured compounds: (a) $(CH_3NH_3)_2Sn(OCN)_2Br_2$, (b) $(CH_3NH_3)_2Sn(SeCN)_2Br_2$, (c) $(CH_3NH_3)_2Sn(OCN)_2I_2$, and (d) $(CH_3NH_3)_2Sn(SeCN)_2I_2$. The valence band maximum is set to 0 eV. Valence and conduction bands indicated by blue and orange lines, respectively. Green and red circles indicate the valence band maximum and conduction band minimum.

the pseudohalides, the primary difference in the band structures is a dramatic reduction in the valence bandwidth, with the conduction band also affected to a lesser extent. This effect is particularly apparent in the chlorides and bromides but is considerably reduced in the iodides. The in-plane hole effective masses are also strongly affected by the choice of pseudohalide, with OCN generally resulting in masses around twice as heavy as those seen in the SCN and SeCN analogues. The anisotropy of the Rashba splitting in the conduction band is affected considerably more by the pseudohalides than the halides, with the lopsided spin-split pockets seen in the cyanates becoming more symmetrical in the thiocyanates and selenocyanates. As the conduction band is composed of metal p states, this asymmetry is likely due to distortion of the local symmetry around the metal site. Indeed, analysis of the crystal structures reveals that OCN incorporation leads to greater off-centring of the metal cation within the MX_4Ps_2 octahedra than SCN and SeCN. This distortion can be attributed to the formation of a stereochemically active lone-pair of electrons on the Sn ($5s^2$) or Pb ($6s^2$) sites, the activity of which, according the revised lone-pair model, will be strongest for OCN and weaker for SCN and SeCN.[73,74]

Taken together, these results reveal a particular pattern: for the chlorides and bromides, moving down the pseudohalides results in reduced band gaps and considerably narrower valence bandwidths. In the iodides, however, these trends are not obeyed and, in some cases, are even reversed. This discrepancy can be explained through analysis of the relative energies of the halide and pseudohalide p orbitals. For the pseudohalides, the chalcogenide p orbitals are of primary concern considering their

direct bonding to the metal cation. In the cyanates, the O p orbitals are found $\sim$1–2 eV below the VBM, resulting in an upper valence band composed predominantly of halide p and metal s states (Fig. 4a). The effective masses, valence bandwidths and band gaps of the cyanates are therefore controlled by the halide, with smaller effective masses seen in the iodides than the chlorides and bromides due to greater localisation of the Cl 3p and Br 4p orbitals. In the thiocyanates and selenocyanates, the chalogen p states (10.4 eV and 9.8 eV for the S 3p and Se 4p, respectively)[75] are higher in energy the chloride and bromide p states (ionisation potential = 13.0 eV and 11.8 eV, respectively),[75] such that they dominate the valence band maximum, resulting in reduced dispersion and bandwidth due to their greater localisation (Fig. 4b). However, in the iodides, the binding energy of the I 5p orbitals (10.4 eV)[75] is sufficiently high in energy that it can hybridise with the S and Se p states, thereby maintaining a consistent band gap across the pseudohalides, with only limited reduction in the valence bandwidth.

The dielectric constants for the full range of analogues, calculated using PBEsol, are provided in Table 2. In general, the dielectric constants for the direction perpendicular to the perovskite sheets are smaller and show less variation ($\varepsilon_r^{\perp}$ = 6.4–12.5) than for the directions parallel to the sheets ($\varepsilon_r^{\parallel}$ = 6.1–21.9). The lead analogues, on average, show larger dielectric constants than their tin counterparts, as expected due to the greater polarisability of the Pb^{2+} cation. Within the lead analogues, the choice of halide appears to have the largest effect on $\varepsilon_r^{\parallel}$, with the chlorides possessing considerably smaller constants ($\sim$10) than the bromides ($\sim$18) and iodides ($\sim$20).
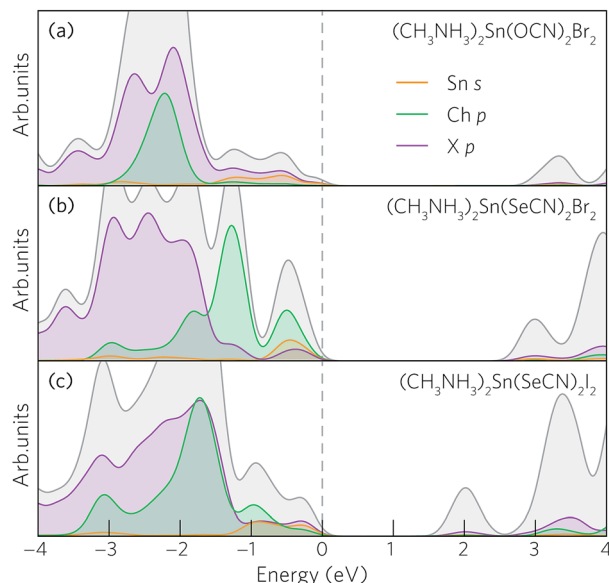
Fig. 4 Projected density of states for (a) $(CH_3NH_3)_2Sn(OCN)_2Br_2$, (b) $(CH_3NH_3)_2Sn(SeCN)_2Br_2$, and (c) $(CH_3NH_3)_2Sn(SeCN)_2I_2$, highlighting the relative contributions of the chalcogenide (Ch) and halide (X) to the upper valence band. The valence band maximum is set to 0 eV and is indicated by a dashed line. The contributions of the N, C, and Sn p orbitals have been omitted for clarity.

The tin analogues show a slightly different trend, with the in-plane dielectric constant largest for the iodides (∼12–20) and smaller for the chlorides (∼7) and bromides (∼8). Overall, the relatively large dielectric constants of the iodides are expected be ideal for solar cell applications, where greater charge screening should reduce defect binding energies and promote the formation of shallower defects.[76,77]

3.3 Band alignments

Close band alignment of the absorber layer with hole and electron contact materials is essential to achieve optimal efficiencies in functioning solar devices.[4] The ionisation potential

(the energy gap between the valence band maximum and the vacuum level) and electron affinity (the energy gap between the conduction band minimum and the vacuum level) of a compound will also play a role in determining its dopability—a measure of the ease of n or p type doping.[78] Across MAPSI and its analogues, the electron affinity (EA) shows significantly less variation than the ionisation potential (IP) (Fig. 5). As such, the position of the valence band maximum, and, therefore, the choice of halide, is the primary factor controlling the magnitude of the band gap. As expected based on our previous bonding analysis, the ionisation potential and electron affinity stay more or less constant when comparing equivalent (i.e. those with the same halide and metal composition) SCN and SeCN analogues. The EA and IP of the lead analogues are slightly larger than their tin counterparts, reflecting the greater stability of the Pb s and p states due to enhanced relativistic effects. The larger IP of the lead compounds is expected to confer a greater resistance to oxidation, whereas the larger EA should allow for increased ease of n-type doping, relative to the tin analogues.

The calculated ionisation potential of MAPSI (5.6 eV) shows excellent agreement with experimental results (5.7 eV).[33] As expected due to the similarities in valence band composition, the ionisation potential of MAPSI is close to that of MAPI (5.5–5.7 eV).[2,79] This suggests that devices containing the lead iodide analogues should perform favourably with spiro-OMeTAD (IP = 5.2 eV),[2] the most commonly used hole transporting layer in MAPI devices. Furthermore, the electron affinity of the lead iodide analogues (3.7–3.9 eV) allows for an efficient match with fluorine-doped tin oxide (FTO, EA = 4.4 eV),[80] a readily available and relatively cheap transparent conducting oxide.

3.4 Intrinsic defects

Whether a material will possess intrinsic p- or n-type conductivity depends on the presence of defects in the system. As such, the defect properties play a crucial role in determining how a photovoltaic absorber will perform in practice. We have therefore examined a range of intrinsic donor and acceptor
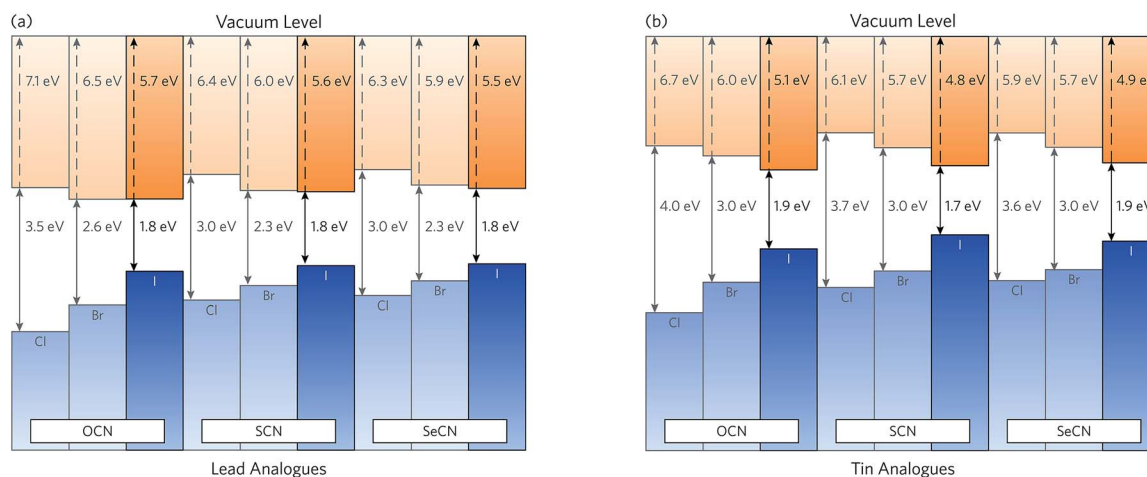

Fig. 5 Band alignment of (a) $(CH_3NH_3)_2PbPs_2X_2$ and (b) $(CH_3NH_3)_2SnPs_2X_2$ (where Ps = OCN, SCN, SeCN; and X = Cl, Br, I), relative to the vacuum level. Ionisation potentials and band gaps indicated by dashed and solid lines, respectively.

vacancy defects in MAPSI and its analogues, comprising two halide vacancies (one for each symmetry inequivalent iodine site), V_I^1 and V_I^2, a pseudohalide vacancy, V_{SCN}, a methylammonium vacancy, V_{MA}, and a metal vacancy, V_{Pb}. The charge-state transition level diagram of MAPSI, calculated using PBEsol, is displayed in Fig. 6a.

Of the two V_I defects, one possesses a very shallow 0/+1 transition level 0.01 eV below the CBM, whereas the other shows a slightly less shallow transition state 0.15 eV below the CBM. The donor defect, V_{SCN}, is also completely resonant in the conduction band. Of the acceptor defects, V_{MA} is resonant in the valence band, highlighting the highly ionic nature of the MA$^+$ cation. V_{Pb} on the other hand shows a relatively shallow $-1/0$ transition state 0.11 eV above the valence band but an ultradeep $-2/-1$ transition state 0.52 eV below the CBM that may act as a recombination centre. We note that while our prediction of

shallow transition levels for the V_I, V_{SCN}, and V_{MA} defects is in qualitative agreement with previous reports in the literature, our identification of an ultradeep V_{Pb} $-2/-1$ transition level is at variance to the results of Xiao *et al.* who instead found this transition level 0.44 eV above the VBM.[40] This discrepancy may result from several factors including the larger supercell size used in our calculations (450 *versus* 400 atoms), our tighter geometry relaxation criterion (0.01 eV Å^{-1} *versus* 0.05 eV Å^{-1}), or the difference in functional (PBEsol *versus* PBE).

Upon moving to other pseudohalides, the defect chemistry remains almost unchanged, as evidenced by the charge-state transition level diagram of MA$_2$Pb(OCN)$_2$I$_2$ shown in Fig. 6b (the transition level diagrams for all iodide analogues are provided in Fig. S4 of the ESI†). The iodide vacancies show relatively shallow 0/+1 transition levels 0.16 eV and 0.08 eV below the CBM, with V_{OCN} and V_{MA} resonant in the conduction and valence bands, respectively. Again, only the V_{Pb} $-2/-1$ transition level is present deep in the band gap and may therefore play a role in trap-assisted recombination. Replacing lead with tin results in deeper iodide vacancies (0.15 eV and 0.32 eV) with the rest of the defects remaining relatively unaffected, as demonstrated in the charge-state transition level diagram of MA$_2$Sn(SCN)$_2$I$_2$ (Fig. 6c).

4 Conclusion

We have demonstrated, using relativistic density functional theory, that the electronic properties of MAPSI can be tuned through incorporation of different halides, pseudohalides and metal cations. All compounds in the series (CH$_3$NH$_3$)$_2$MPs$_2$X$_2$, where M = Pb, Sn; Ps = OCN, SCN, SeCN; and X = Cl, Br, I, retain the orthorhombic structural motif of MAPSI and possess close-to-direct band gaps, controlled largely by the choice of halide. Similar to MAPSI, all analogues were found to be stable with respect to phase separation. Furthermore, band alignments indicate favourable matching with hole and electron contact materials commonly used in the production of MAPI based solar cells. The iodide analogues, due to their suitable band gaps and relatively large dielectric constants, show promise for the future of all perovskite tandem devices. In particular, the possibility of lead-free MAPSI analogues presents an exciting prospect due to concerns over the toxicity of lead in the hybrid-halide perovskites, and we therefore welcome experimental verification of our results.

Acknowledgements
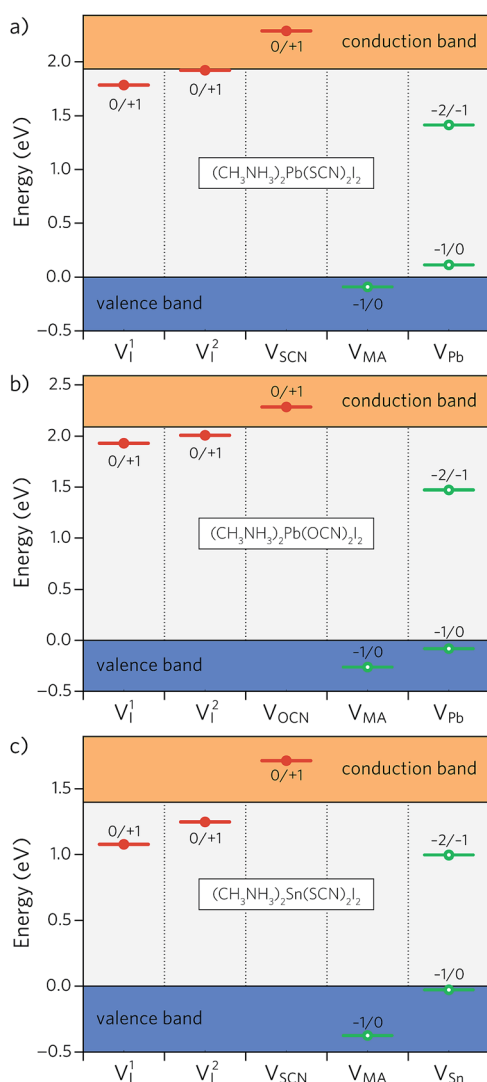
Fig. 6 Calculated charge-state transition level diagram for a range of intrinsic vacancy defects in (a) (CH$_3$NH$_3$)$_2$Pb(SCN)$_2$I$_2$, (b) (CH$_3$NH$_3$)$_2$Pb(OCN)$_2$I$_2$, and (c) (CH$_3$NH$_3$)$_2$Sn(SCN)$_2$I$_2$ calculated at the PBEsol level. Red bands with filled circles indicate donor defects, green bands with open circles indicate acceptor defects.

References

1 M. Grätzel, *Nat. Mater.*, 2014, **13**, 838–842.

2 M. A. Green, A. Ho-Baillie and H. J. Snaith, *Nat. Photonics*, 2014, **8**, 506–514.

3 N.-G. Park, *J. Phys. Chem. Lett.*, 2013, **4**, 2423–2429.

4 A. M. Ganose, C. N. Savory and D. O. Scanlon, *Chem. Commun.*, 2016, **53**, 20–44.

5 T. Baikie, Y. Fang, J. M. Kadro, M. Schreyer, F. Wei, S. G. Mhaisalkar, M. Graetzel and T. J. White, *J. Mater. Chem. A*, 2013, **1**, 5628–5641.

6 V. D'Innocenzo, G. Grancini, M. J. Alcocer, A. R. S. Kandada, S. D. Stranks, M. M. Lee, G. Lanzani, H. J. Snaith and A. Petrozza, *Nat. Commun.*, 2014, **5**, 3586.

7 C. Wehrenfennig, G. E. Eperon, M. B. Johnston, H. J. Snaith and L. M. Herz, *Adv. Mater.*, 2014, **26**, 1584–1589.

8 Y. Zhao and K. Zhu, *J. Phys. Chem. Lett.*, 2013, **4**, 2880–2884.

9 Y. Deng, E. Peng, Y. Shao, Z. Xiao, Q. Dong and J. Huang, *Energy Environ. Sci.*, 2015, **8**, 1544–1550.

10 G. Xing, N. Mathews, S. Sun, S. S. Lim, Y. M. Lam, M. Gratzel, S. Mhaisalkar and T. C. Sum, *Science*, 2013, **342**, 344–347.

11 A. Walsh, D. O. Scanlon, S. Chen, X. Gong and S.-H. Wei, *Angew. Chem.*, 2015, **127**, 1811–1814.

12 A. T. Barrows, A. J. Pearson, C. K. Kwak, A. D. F. Dunbar, A. R. Buckley and D. G. Lidzey, *Energy Environ. Sci.*, 2014, **7**, 2944.

13 D. S. Bhachu, D. O. Scanlon, E. J. Saban, H. Bronstein, I. P. Parkin, C. J. Carmalt and R. G. Palgrave, *J. Mater. Chem. A*, 2015, **3**, 9071–9073.

14 G. Hodes and D. Cahen, *Nat. Photonics*, 2014, **8**, 87–88.

15 K. Leo, *Nat. Nanotechnol.*, 2015, **10**, 574–575.

16 J. A. Christians, J. S. Manser and P. V. Kamat, *J. Phys. Chem. Lett.*, 2015, **6**, 852–857.

17 B. Conings, J. Drijkoningen, N. Gauquelin, A. Babayigit, J. D'Haen, L. D'Olieslaeger, A. Ethirajan, J. Verbeeck, J. Manca, E. Mosconi, F. D. Angelis and H.-G. Boyen, *Adv. Energy Mater.*, 2015, **5**, 1500477.

18 E. J. Juarez-Perez, Z. Hawash, S. R. Raga, L. K. Ono and Y. Qi, *Energy Environ. Sci.*, 2016, **9**, 3406–3410.

19 G. Niu, W. Li, F. Meng, L. Wang, H. Dong and Y. Qiu, *J. Mater. Chem. A*, 2014, **2**, 705–710.

20 A. Pisoni, J. Jaćimović, O. S. Barišić, M. Spina, R. Gaál, L. Forró and E. Horváth, *J. Phys. Chem. Lett.*, 2014, **5**, 2488–2492.

21 Y.-Y. Zhang, S. Chen, P. Xu, H. Xiang, X.-G. Gong, A. Walsh and S.-H. Wei, arXiv:1506.01301 [cond-mat.mtrl-sci], 2015.

22 A. M. Ganose, C. N. Savory and D. O. Scanlon, *J. Phys. Chem. Lett.*, 2015, **6**, 4594–4598.

23 S. Guarnera, A. Abate, W. Zhang, J. M. Foster, G. Richardson, A. Petrozza and H. J. Snaith, *J. Phys. Chem. Lett.*, 2015, **6**, 432–437.

24 G. Niu, X. Guo and L. Wang, *J. Mater. Chem. A*, 2015, **3**, 8970–8980.

25 W. Travis, E. Glover, H. Bronstein, D. Scanlon and R. Palgrave, *Chem. Sci.*, 2016, **7**, 4548–4556.

26 C. N. Savory, A. Walsh and D. O. Scanlon, *ACS Energy Lett.*, 2016, **1**, 949–955.

27 K. Gregor, S. Shijing and K. C. Anthony, *Chem. Sci.*, 2014, **5**, 4712–4715.

28 G. Kieslich, S. Sun and T. Cheetham, *Chem. Sci.*, 2015, **6**, 3430–3433.

29 L. N. Quan, M. Yuan, R. Comin, O. Voznyy, E. M. Beauregard, S. Hoogland, A. Buin, A. R. Kirmani, K. Zhao, A. Amassian, D. H. Kim and E. H. Sargent, *J. Am. Chem. Soc.*, 2016, **138**, 2649–2655.

30 D. B. Mitzi, *Chem. Mater.*, 1996, **8**, 791–800.

31 N. Kitazawa and Y. Watanabe, *J. Phys. Chem. Solids*, 2010, **71**, 797–802.

32 Q. Jiang, D. Rebollar, J. Gong, E. L. Piacentino, C. Zheng and T. Xu, *Angew. Chem., Int. Ed.*, 2015, **54**, 7617–7620.

33 J. Liu, J. Shi, D. Li, F. Zhang, X. Li, Y. Xiao and S. Wang, *Synth. Met.*, 2016, **215**, 56–63.

34 M. Daub and H. Hillebrecht, *Angew. Chem.*, 2015, **127**, 11168–11169.

35 Y. Chen, B. Li, W. Huang, D. Gao and Z. Liang, *Chem. Commun.*, 2015, **51**, 11997–11999.

36 Z. Xiao, W. Meng, B. Saparov, H.-S. Duan, C. Wang, C. Feng, W.-Q. Liao, W. Ke, D. Zhao, J. Wang, D. B. Mitzi and Y. Yan, *J. Phys. Chem. Lett.*, 2016, **7**, 1213–1218.

37 D. Umeyama, Y. Lin and H. I. Karunadasa, *Chem. Mater.*, 2016, **28**, 3241–3244.

38 R. Younts, H.-S. Duan, B. Gautam, B. Saparov, J. Liu, C. Mongin, F. N. Castellano, D. B. Mitzi and K. Gundogdu, *Adv. Mater.*, 2017, 1604278.

39 K. A. Bush, A. F. Palmstrom, Z. J. Yu, M. Boccard, R. Cheacharoen, J. P. Mailoa, D. P. McMeekin, R. L. Z. Hoye, C. D. Bailie, T. Leijtens, I. M. Peters, M. C. Minichetti, N. Rolston, R. Prasanna, S. Sofia, D. Harwood, W. Ma, F. Moghadam, H. J. Snaith, T. Buonassisi, Z. C. Holman, S. F. Bent and M. D. McGehee, *Nat. Energy*, 2017, 1–7.

40 Z. Xiao, W. Meng, J. Wang and Y. Yan, *Phys. Chem. Chem. Phys.*, 2016, **18**, 25786–25790.

41 P. Azarhoosh, J. M. Frost, S. McKechnie, A. Walsh and M. van Schilfgaarde, *APL Mater.*, 2016, **4**, 091501.

42 T. Etienne, E. Mosconi and F. D. Angelis, *J. Phys. Chem. Lett.*, 2016, **7**, 1638–1645.

43 A. Walsh, *J. Mater. Chem. C*, 2015, **119**, 5755–5760.

44 C. C. Stoumpos, L. Mao, C. D. Malliakas and M. G. Kanatzidis, *Inorg. Chem.*, 2017, **56**, 56–73.

45 G. Kresse and J. Hafner, *Phys. Rev. B: Condens. Matter Mater. Phys.*, 1993, **47**, 558–561.

46 G. Kresse and J. Hafner, *Phys. Rev. B: Condens. Matter Mater. Phys.*, 1994, **49**, 14251–14269.

47 G. Kresse and J. Furthmüller, *Phys. Rev. B: Condens. Matter Mater. Phys.*, 1996, **54**, 11169–11186.

48 G. Kresse and J. Furthmüller, *Comput. Mater. Sci.*, 1996, **6**, 15.

49 G. Kresse, *Phys. Rev. B: Condens. Matter Mater. Phys.*, 1999, **59**, 1758–1775.

50 P. Pulay, *Mol. Phys.*, 1969, **17**, 197–204.

7852 | *J. Mater. Chem. A*, 2017, **5**, 7845–7853

This journal is © The Royal Society of Chemistry 2017

51 J. P. Perdew, A. Ruzsinszky, G. I. Csonka, O. A. Vydrov, G. E. Scuseria, L. A. Constantin, X. Zhou and K. Burke, *Phys. Rev. Lett.*, 2008, **100**, 136406.

52 J. P. Perdew, K. Burke and M. Ernzerhof, *Phys. Rev. Lett.*, 1996, **77**, 3865–3868.

53 T. Björkman, *Phys. Rev. B: Condens. Matter Mater. Phys.*, 2012, **86**, 165109.

54 A. M. Ganose, K. T. Butler, A. Walsh and D. O. Scanlon, *J. Mater. Chem. A*, 2016, **4**, 2060–2068.

55 A. V. Krukau, O. A. Vydrov, A. F. Izmaylov and G. E. Scuseria, *J. Chem. Phys.*, 2006, **125**, 224106.

56 C. N. Savory, A. M. Ganose, W. Travis, R. S. Atri, R. G. Palgrave and D. O. Scanlon, *J. Mater. Chem. A*, 2016, **4**, 12648–12657.

57 D. Hobbs, G. Kresse and J. Hafner, *Phys. Rev. B: Condens. Matter Mater. Phys.*, 2000, **62**, 11556–11570.

58 C. H. Hendon, R. X. Yang, L. A. Burton and A. Walsh, *J. Mater. Chem. A*, 2015, **3**, 9067–9070.

59 A. E. Maughan, A. M. Ganose, M. M. Bordelon, E. M. Miller, D. O. Scanlon and J. R. Neilson, *J. Am. Chem. Soc.*, 2016, **138**, 8453–8464.

60 W. Travis, C. E. Knapp, C. N. Savory, A. M. Ganose, P. Kafourou, X. Song, Z. Sharif, J. K. Cockcroft, D. O. Scanlon, H. Bronstein, *et al.*, *Inorg. Chem.*, 2016, **55**, 3393–3400.

61 K. T. Butler, J. M. Frost and A. Walsh, *Mater. Horiz.*, 2015, **2**, 228–231.

62 C. N. Savory, R. G. Palgrave, H. Bronstein and D. O. Scanlon, *Sci. Rep.*, 2016, **6**, 20626.

63 S. Baroni, S. De Gironcoli, A. Dal Corso and P. Giannozzi, *Rev. Mod. Phys.*, 2001, **73**, 515.

64 Z. Yang, C.-C. Chueh, F. Zuo, J. H. Kim, P.-W. Liang and A. K.-Y. Jen, *Adv. Energy Mater.*, 2015, **5**, 1500328.

65 A. Walsh, A. B. Kehoe, D. J. Temple, G. W. Watson and D. O. Scanlon, *Chem. Commun.*, 2013, **49**, 448–450.

66 L. A. Burton and A. Walsh, *Appl. Phys. Lett.*, 2013, **102**, 132111.

67 A. M. Ganose, M. Cuff, K. T. Butler, A. Walsh and D. O. Scanlon, *Chem. Mater.*, 2016, **28**, 1980–1984.

68 S. Lany and A. Zunger, *Phys. Rev. B: Condens. Matter Mater. Phys.*, 2008, **78**, 17–20.

69 C. Freysoldt, B. Grabowski, T. Hickel, J. Neugebauer, G. Kresse, A. Janotti and C. G. Van De Walle, *Rev. Mod. Phys.*, 2014, **86**, 253–305.

70 C. Freysoldt, J. Neugebauer and C. G. Van de Walle, *Phys. Rev. Lett.*, 2009, **102**, 016402.

71 S. T. Murphy and N. D. M. Hine, *Phys. Rev. B: Condens. Matter Mater. Phys.*, 2013, **87**, 1–6.

72 https://github.com/SMTG-UCL/MAPSI, accessed: 22-02-2017.

73 D. J. Payne, R. G. Egdell, A. Walsh, G. W. Watson, J. Guo, P. A. Glans, T. Learmonth and K. E. Smith, *Phys. Rev. Lett.*, 2006, **96**, 157403.

74 A. Walsh, D. J. Payne, R. G. Egdell and G. W. Watson, *Chem. Soc. Rev.*, 2011, **40**, 4455–4463.

75 R. C. Weast, M. J. Astle and W. H. Beyer, *et al.*, *CRC handbook of chemistry and physics*, CRC Press, Boca, Raton, FL, 1986, vol. 66.

76 R. H. Bube, *Photoelectronic Properties of Semiconductors*, Cambridge University Press, 1992.

77 Y. Peter and M. Cardona, *Fundamentals of semiconductors: physics and materials properties*, Springer Science & Business Media, 2010.

78 A. M. Ganose and D. O. Scanlon, *J. Mater. Chem. C*, 2016, **4**, 1467–1475.

79 J. M. Frost, K. T. Butler, F. Brivio, C. H. Hendon, M. Van Schilfgaarde and A. Walsh, *Nano Lett.*, 2014, **14**, 2584–2590.

80 M. Helander, M. Greiner, Z. Wang, W. Tang and Z. Lu, *J. Vac. Sci. Technol., A*, 2011, **29**, 011019.

This journal is © The Royal Society of Chemistry 2017

J. Mater. Chem. A, 2017, **5**, 7845–7853 | **7853**